FULL PAPER

Combined application of isotropic three-dimensional fast spin echo (3D-FSE-Cube) with 2-point Dixon fat/water separation (FLEX) and 3D-FSE-cube in MR dacryocystography

[1]PING LIU, [1]QIUXIA WANG, [1]CHENGDONG PENG, [2]BAN LUO, MD and [1]JING ZHANG, MD, PhD

[1]Department of Radiology, The Affliated Tongji Hospital, Tongji Medical College, Huazhong University of Science & Technology, Wuhan, China
[2]Department of Ophtalmology, The Affliated Tongji Hospital, Tongji Medical College, Huazhong University of Science & Technology, Wuhan, China

Address correspondence to: Dr Jing Zhang
E-mail: hbclleo@163.com

The authors Ping Liu and Qiuxia Wang contributed equally to the work.

Objective: To evaluate the image quality of magnetic resonance dacryocystography (MRD) using three-dimensional fast spin-echo -Cube (3D-FSE-Cube) and 3D-FSE-Cube-Flex sequences to examine the lacrimal drainage system (LDS).

Methods: 21 healthy volunteers underwent 3D-FSE-Cube and 3D-FSE-Cube-Flex MRD after topical administration of compound sodium chloride eye drops. Two radiologists assessed LDS images in a blinded fashion. The signal-to-noise ratio of fluid-filling and the contrast-to-noise ratio of fluid-turbinate were compared between the two sequences. Overall image quality, sharpness, artefacts, visualization of anatomical structures, and visibility of LDS segments were also compared.

Results: Overall image quality, visualization of anatomic structures, and artefact were significantly better on 3D-FSE-Cube-Flex MRD ($p < 0.001$, respectively). when compared to 3D-FSE-Cube. 3D-FSE-Cube showed lower fluid-filling signal-to-noise ratio and fluid-inferior turbinate CNR (all $p < 0.001$). In comparison with 3D-FSE-Cube-Flex, 3D-FSE-Cube produced superior visibility of the upper drainage segments (superior canaliculi, $p = 0.003$; common canaliculus, $p = 0.033$; inferior canaliculi, $p < 0.001$), but inferior in lower-LDS visibility (lacrimal sac, $p = 0.001$; nasolacrimal duct, $p < 0.001$). There was no difference in the total number of segments visualized per LDS between the two sequences ($p = 0.068$).

Conclusions: 3D-FSE-Cube-Flex demonstrated superior image quality and visibility of the lower LDS segments. 3D-FSE-Cube showed an advantage in visualizing the upper LDS segments. The combination of these sequences can improve LDS visibility.

Advances in knowledge: 3D-FSE-Cube-Flex provides robust water & fat separation and mitigates lower LDS-associated inhomogeneity artefacts. 3D-FSE-Cube shows optimal upper LDS visualization. The combined application of these sequences is a non-invasive and effective method for assessing LDS disease.

INTRODUCTION

Human lacrimal drainage system (LDS) consists of five segments: the superior canaliculus (SC), inferior canaliculus (IC), common canaliculus (CC), lacrimal sac (LS), and the nasolacrimal duct (NLD).[1] The upper LDS segments (SC, IC, and CC) and the lower LDS segments (LS and NLD) are in a near vertical orientation, with the upper segments arranged are horizontally, whereas the lower segments are oriented at small angles to either the coronal or sagittal plane.[2] Clear and exact image information is crucial for the clinician to achieve an effective therapeutic plan, particularly in patients prior to surgery. Magnetic resonance dacryocystography (MRD) using a topical instillation of saline solution has been reported in several studies.[3,4] Continuous and slow-moving liquid is used instead of contrast media in MRD has been shown to be safe with no side effects, and hyperintense signal from fluid-filling in cavities can delineate the lacrimal passage on T_2 weighted MRI. Recently, Francesco et al[5] showed that unenhanced MRI was highly reliable and even more

Table 1. Parameters of 3D-FSE-Cube MRD and 3D-FSE-Cube-Flex MRD

Sequences	TR (ms)	eff TE (ms)[a]	NEX	Acc	ETL	Matrix	FOV (cm)	Thickness/space (mm)	RBW (kHz)	TA(min:s)
3D-FSE-Cube	3000	98.7	2	3	128	256 × 256	25.6	1/0	62.5	6:49
3D-FSE-Cube-Flex	2000	107	1	3	120	256 × 256	26.6	1/0	83.3	6:35

Acc, acceleration factor; Eff TE,effective echo time; ETL, echo-train length; FOV, field of view; NEX, number of excitation; TA, acquisition time; TR, repetition time; RBW, receiver bandwidth.
Thickness/space = Slice thickness/slice space.
[a]for 3D-FSE-Cube-Flex, the delta TE(TE) is around 1.05 ms.

effective than enhanced MRI for the preoperative characterization of NLD stenosis. Three-dimensional (3D) fast-recovery fast spin-echo (FRFSE) combines the topical instillation of saline water provided both morphological and functional information of LDSs, but failed to delineate more anatomical details, including the surrounding structures.[6] 3D-FSE-Cube, with the administration of compound sodium chloride eye drops, plays a role in hydrography and yields good soft-tissue contrast, which directly reveals the position and morphology of LDSs by arbitrary orientation–reconstruction.[7,8] However, this technique is prone to produce images with hypointense fissure artefacts blended with a hyperintense lachrymal sac and/or NLD,[6] which affects visualization of the ductal wall. The primary cause of this artefact may be due to complicated periphery structures of the LDSs (*e.g.* periorbital fat, paranasal sinuses, as well as air in the nasal cavities etc.), which can lead to a non-uniform magnetic field. Additionally, the optional chemically selective fat suppression (CHESS) method exploited in 3D-FSE-Cube using fat-selective radiofrequency (RF) pulses to achieve fat suppression, which is sensitive to B0 (magnetic field) and B1(RF pulse) field inhomogeneities,[9,10] this vulnerability is more prominent at 3.0 T than at lower magnetic field strengths,[11] thereby aggravating inhomogeneity artefacts.

The Dixon method is a classical technique for generating homogeneous "fat-suppression," or "water-fat separation" images. 3D-FSE combined with the Dixon method for water–fat separation has been successfully and widely used in various parts of the body, such as the breast,[12] abdomen,[13,14] musculoskeletal tissue,[15–18] brachial plexus,[19] and the prostate.[20] These applications have demonstrated that this integration has advantages in optimizing the contrast-to-noise ratio (CNR) offering signal-to-noise ratio (SNR)-efficient and robust fat suppression images, which may better define lesions while reducing artefacts sensitive to an inhomogeneous magnetic field on water-only images. Flex (GE Healthcare, Milwaukee, WI) is a modified two-point technique for fat–water separation and is usually used when image acquisition speed is important.[21] Cube-Flex incorporates a 3D-FSE acquisition and a two-point Dixon method. We postulate that this combination can generate high-resolution water–fat separation images in presence of B0 inhomogeneity, the water-only images acquired by 3D-FSE-Cube Flex may partially address the deficiencies that occur in 3D-FSE-Cube images. The aim of this study was to compare image quality and the visibility of the LDS using MRD imaging acquired with either 3D-FSE-Cube or 3D-FSE-Cube-Flex in healthy volunteers.

METHODS AND MATERIALS
Patients
Institutional review board approval was obtained from our institutional ethics committee, and this study was compliant with the Helsinki II declaration. We randomly recruited 21 healthy volunteers (8 females, 13 males) among workmates and trainees in our department, with the average age of the participants being 30.1 years (range, 22.0–46.0 years). All study subjects provided written informed consent prior to examination. In this preliminary study, we primarily aimed to demonstrate the differences between Cube-MRD and Cube-flex MRD under normal

Figure 1. Examples of ROI placement for filling-fluid[1] and noise.[2] ROI, region of interest.
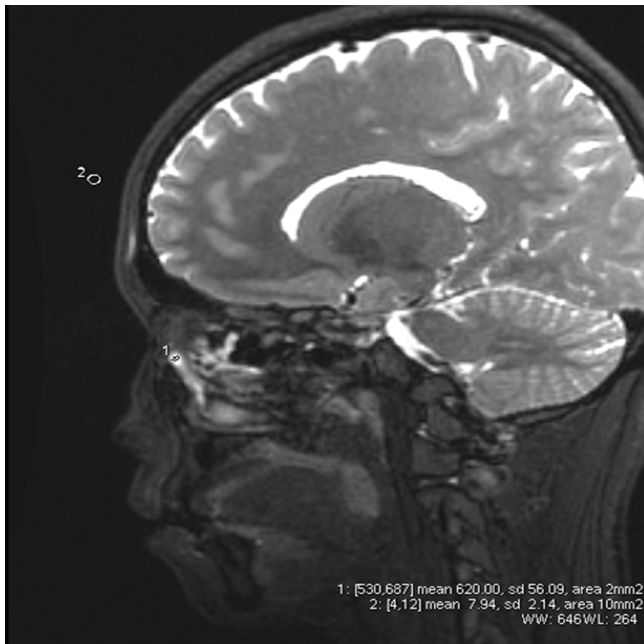
circumstances. Therefore, we recruited young healthy adults who had no history of dental restoration or maxillofacial plastic surgery for this study.

MRI

Imaging was performed on a 3.0 T MRI system (Signa HDxt, GE Healthcare), using a standard head coil (8-channel HD Brain Coil, GE Healthcare). The MRI protocol consisted of 3D-FSE-Cube and 3D-FSE-Cube-Flex acquired MRD. Before and during MRI examination, compound sodium chloride eye drops were administrated into both conjunctival sacs, with the specific method identical to previous reports.[6–8]

All the volunteers successfully finished MRI examination, with 42 LDS data sets acquired. The parameters of the 3D-FSE-Cube were similar to a previous study,[6,8] and the 3D-FSE-Cube Flex parameters were kept consistent with the 3D-FSE-Cube as far as possible upon the approximate acquisition time. The specific imaging parameters of the above sequences are listed in Table 1.

Image evaluation

All data sets obtained were sent to a computer workstation (Advantage Windows Workstation 4.6; GE Healthcare). Two experienced board-certified radiologists (with approximately 5 and 10 years of experience in Ophthalmology and Otorhinolaryngology imaging, respectively) randomly and independently reviewed all images. Readers were blinded to all identifying information about sequence type. Studies were read in different orders in each session, as follows: (a) alphabetically by name and sequentially by (b) medical record number. If there existed any difference in opinion between the radiologists' interpretations, consensus would be met by discussion. Two data sets were analyzed separately with at least a 2-week interval.

The readers measured and calculated two conventional image quality metrics on the original sagittal images: SNR and CNR. Refer to the methods of Kathryn J et al,[18] the mean signal intensity (SI) from the filling-fluid in the lacrimal passage and the background image noise were measured in all subjects using regions of interest (ROIs). The average area of the circular ROIs for fluid was 2 mm^2. The ROI of background noise was placed over the forehead region of the image with an area of 10 mm^2 (Figure 1), with the standard deviation (SD) of the noise recorded. The computational formula of SNR and CNR were as follows:

$$SNR = SI_{fluid}/SD_{noise}, CNR = (SI_{fluid} - SI_{turbinate})/(SD_{noise})$$

The noise in this formula is the standard deviation of the background noise.

To visualize the LDS, the original sagittal images (1 mm thickness with an in-plane resolution of 1.0×1.0 mm^2) on both sequences were used as a platform for real-time interactive, multiplane reconstruction in arbitrary orientations manipulated by the reviewers. All evaluation was based on 1 mm thick reformatted oblique sagittal and coronal slices along the long axis of the NLD (Figures 2 and 3). Qualitative impressions included overall image quality, presence of artefacts, sharpness, and visualization of anatomical structures. The paired comparison was graded on a subjective 5-point scale from −2 to +2, where a score of −2 indicated image A was much better than image B; a score of −1 indicated image A was somewhat better than image B; a score of 0 meant no distinction between the 2 images; a score of +1 indicated image B was somewhat better than image A; and a score of +2 indicated image B was much better than image A.

The assessment of the visibility of the five LDS segments (SC, IC, CC, LS, and NLD) were also performed on the reconstructed images (Figures 2 and 3). For visibility, CC was assessed dichotomously, with only scores of 0 and 1 being based, Grade 0 is invisible and Grade 1 stands for visible. Each of the other four segments were scored according to the following 4-point scale: Grade 0, completely invisible and no fluid filled; Grade 1, less than half of the passage can be discerned and filled; Grade 2, more than half of the passage was filled and can be visualized faintly; and, Grade 3, clear and full visualized. Ductal visualization analysis was performed on the basis of the number of segments observed per LDS (maximum of five segments per LDS). Ducts that were either mostly or completely visualized (scores equal to or greater than 2) were considered to be visible.

Statistical analysis

Statistical analysis was performed using the SPSS statistical software (v. 21, IBM Corp., Armonk, NY). Conventional interpretations of p-values were used for all statistical tests, with a significance level of $p < 0.05$ being considered statistically significant.

Comparison of fluid SNR and fluid-turbinate CNR between each sequence (3D-FSE Cube, 3D-FSE Cube-Flex) were performed

Figure 2. 3D-FSE-Cube-Flex for a subject in the (a) oblique coronal, (b) and (c) bilateral oblique sagittal planes. Example of 3D-FSE-Cube for a subject reformatted in the (d) oblique coronal, (e) and (f) bilateral oblique sagittal planes. The attached liquid delineates the profile of the bilateral LS and NLD, with the latter sequence showing a sharper boundary. 3D-FSE, three-dimensional-fast spin-echo; LS, lacrimal sac; NLD, nasolacrimal duct.
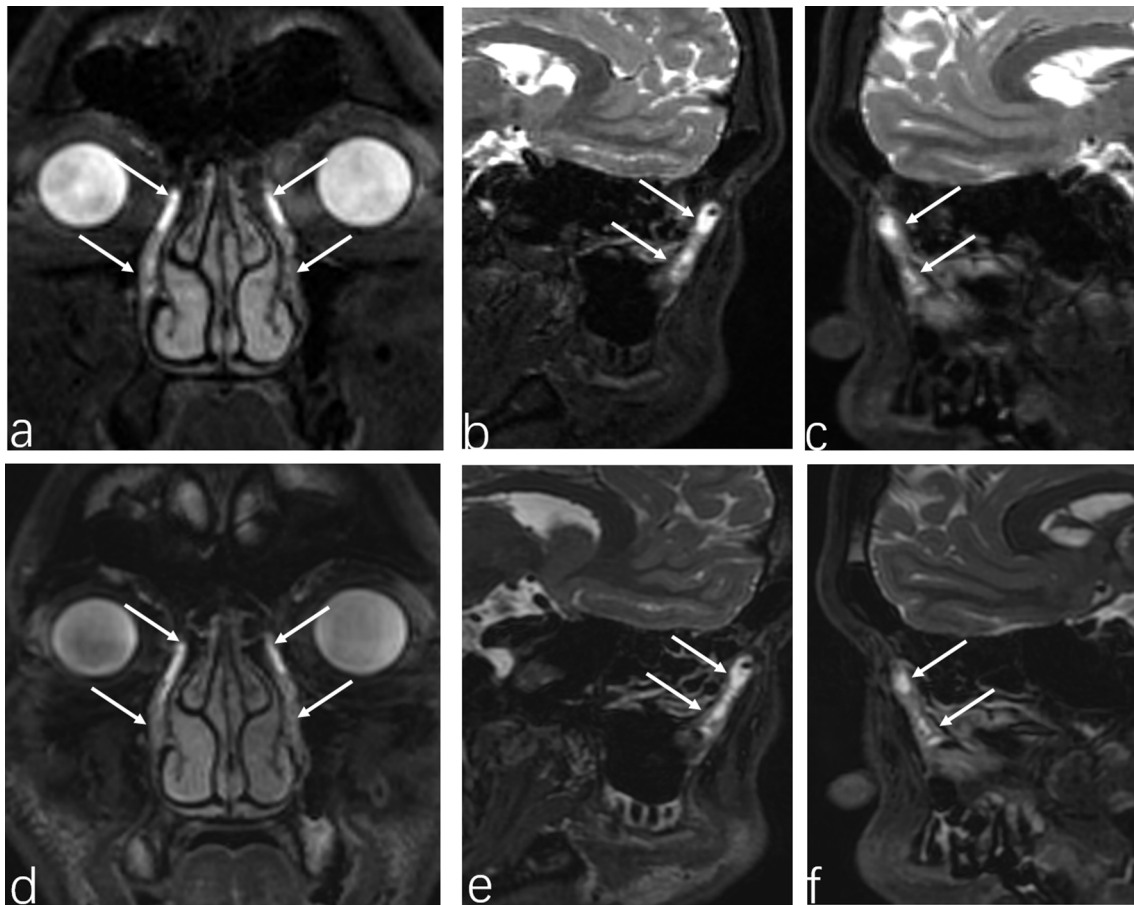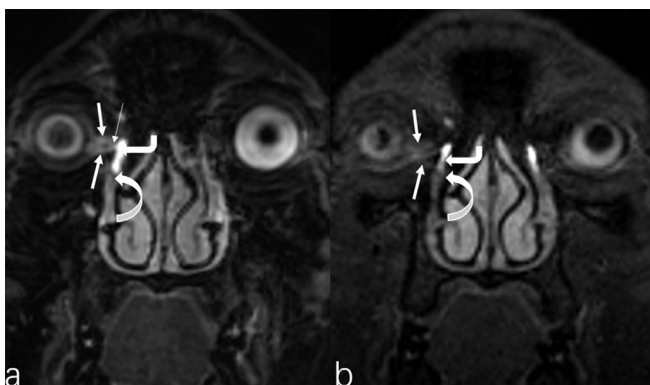

Figure 3. An example of a subject with (A) reformatted oblique coronal 3D-FSE-Cube MRD that clearly delineates the SC and IC (straight arrows), CC (slender white arrow), LS (thick bent arrow), and NLD (curved arrow); and, (B) reformatted oblique coronal 3D-FSE-Cube-Flex MRD, with the CC not visible, as well as the SC and IC are faintly displayed (straight arrows).
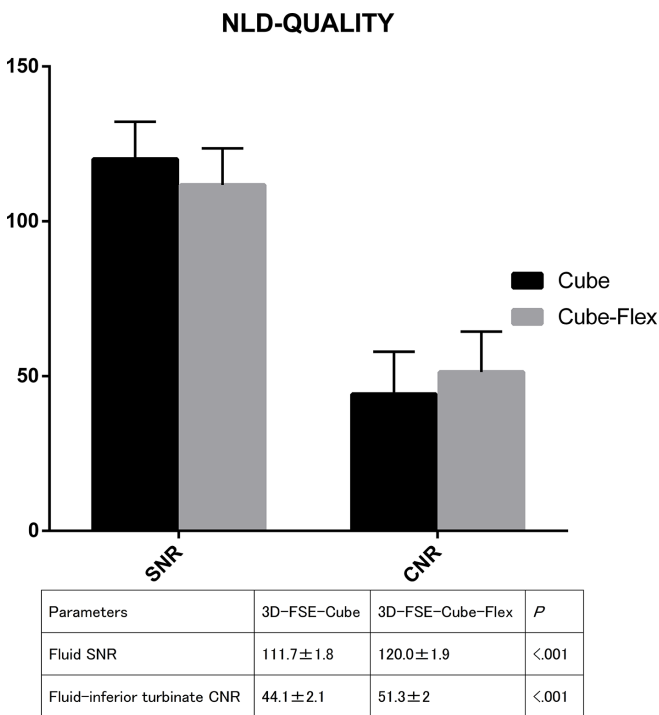

using a paired-sample *t*-test. Mean and standard error of the mean were calculated.

The visibility grade scores of each of the five ductal segments, and the number of visible segments observed per LDS were then compared between the two MRD sequences and analyzed using a two-tailed paired Wilcoxon test.

A two-tailed, paired-sample Wilcoxon signed-rank test was utilized to analyze the difference in other quality metrics (the ratings score of artefacts, overall image quality, sharpness, and visualization of anatomical structures), between the paired images for the non-Gaussian properties of these data sets.

Statistical analysis for inter reader agreement of quality metrics and visibility scores was calculated using the kappa analysis. Intraclass correlation coefficients for SNR and CNR were calculated in order to assess the stability of parameters obtained by the two observers.

Figure 4. The bar chart at the top shows the comparison of SNR of fluid-filling and fluid-inferior turbinate CNR between 3D-FSE-Cube MRD and 3D-FSE-Cube-Flex MRD (mean ± SD). There is a trend toward higher fluid SNR with the 3D-FSE-Cube-Flex over 3D-FSE-Cube, but a contrary tendency in that of CNR in terms of the MRD (*p* < 0.001, respectively). The table below the histogram displays quantitative assessment. Data was presented as mean ± SD and based on all images were obtained with fat-suppression (On 3D-FSE-Cube-Flex, it is mainly the water-only image). *p* < 0.05 was considered statistically significant. 3D-FSE, three-dimensional-fast spin-echo; CNR, contrats-to-noise ratio; MRD, magnetic resonance dacryocystography; NLD, nasolacrimal duct; SD, standard deviation; SNR, signal-to-noise ratio.

NLD-QUALITY

Parameters	3D-FSE-Cube	3D-FSE-Cube-Flex	*P*
Fluid SNR	111.7±1.8	120.0±1.9	<.001
Fluid–inferior turbinate CNR	44.1±2.1	51.3±2	<.001

Figure 5. The histogram displays comparison of the segment visualization scores between 3D-FSE-Cube MRD and 3D-FSE-Cube-Flex MRD, with a trend toward higher scores with superior LDSs for 3D-FSE-Cube MRD, with SC (*p* = 0.003), IC (*p* < 0.001), and CC (*p* = 0.033) being significant. Lower NLDs and the total sections per subject showed a trend with lower rating scores. Data in the table is presented as Mean ± SD and based on all images were obtained with fat-suppression (the water-only images from 3D-FSE-Cube-Flex MRD). The measure of visualization for each ductal section range form 0–3: Grade 0, invisible and no fluid filling; Grade 1, less than half of the passage can be discerned and filled; Grade 2, more than half of the passage was filled and can be faintly visualized; Grade 3, clear and full visualization. *p* < 0.05 was considered statistically significant. 3D-FSE, three-dimensional-fast spin-echo; CC, common canaliculus; IC, inferior canaliculus; LS, lacrimal sac; MRD, magnetic resonance dacryocystography; NLD, nasolacrimal duct; SC, superior canaliculus; SD, standard deviation.

scoring

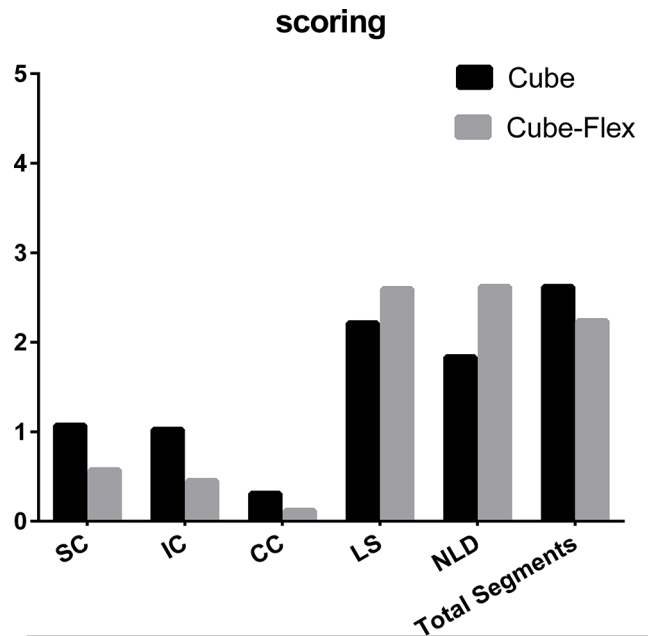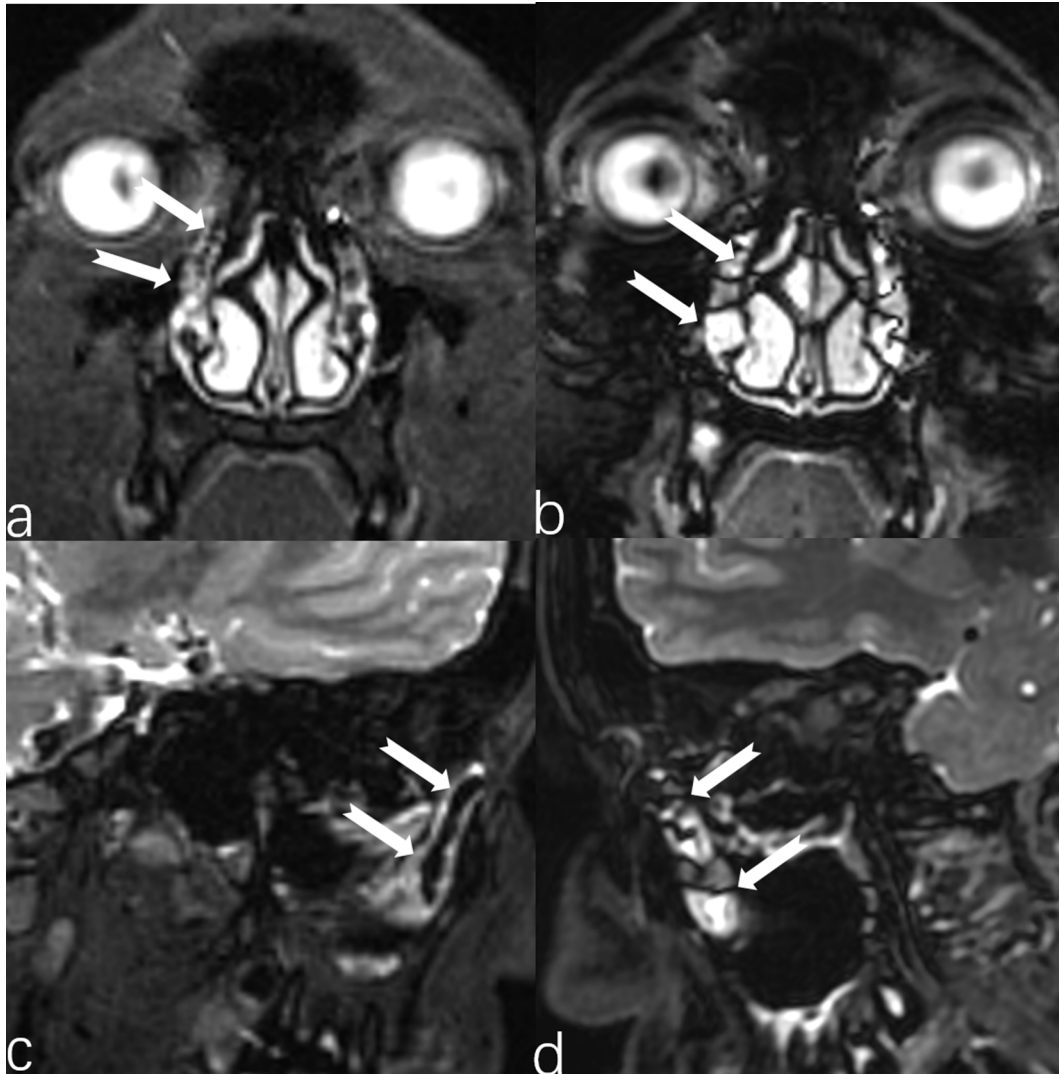|	3D–FSE–Cube	3D–FSE–Cube–Flex	P value
Superior canaliculus	1.1±0.8	0.6±0.7	P=0.003
Inferior canaliculus	1.0±0.8	0.5±0.6	P<0.001
Common canaliculus	0.3±0.5	0.1±0.3	P=0.033
Lacrimal sac	2.2±0.8	2.6±0.6	P=0.001
Nasolacrimal duct	1.8±0.5	2.6±0.5	P<0.001
Total duct segments	2.6±1.3	2.2±0.7	P=0.068

RESULTS

In total, all volunteers successfully finished the imaging protocol, with 42 LDS data sets obtained from 21 subjects, which were evaluated and analyzed. Fluid-filling SNR was significantly higher on MRD scans acquired with 3D-FSE-Cube-Flex (mean, 120.0 ± 1.9), compared to 3D-FSE-Cube (mean, 111.7 ± 1.8, *p* < 0.001). The fluid-inferior turbinate CNR was significantly higher for 3D-FSE-Cube-Flex (mean, 51.3 ± 2.0) than for 3D-FSE-Cube (mean, 44.1 ± 2.1, *p* < 0.001) (Figure 4).

The ductal visualization scores were higher with 3D-FSE-Cube (Figure 3a) than with 3D-FSE-Cube-Flex (Figure 3b), with this difference being statistical significant for SC (1.1 ± 0.8 *vs* 0.6 ± 0.7, respectively, *p* = 0.003), IC (1 ± 0.8*vs*0.5 ± 0.6, respectively, *p* < 0.001), and CC (0.3 ± 0.5*vs*0.1 ± 0.3, *p* = 0.033). Visibility was superior with 3D-FSE-Cube Flex compared with 3D-FSE-Cube for the lower LDS. There was a significant difference for LS (2.6 ± 0.6*vs*2.2 ± 0.8, respectively, *p* = 0.001) and for NLD (2.6 ± 0.5*vs* 1.8 ± 0.5, respectively, *p* < 0.001). Although the number of anatomical segments visualized per LDS was somewhat higher

with 3D-FSE-Cube, the difference between the sequences did not reach statistical significance (*p* = 0.068) (Figure 5).

Better overall image quality was determined for 3D-FSE-Cube-Flex (Z = −4.333, *p* < 0.001). 3D-FSE-Cube-Flex was superior to 3D-FSE-Cube for the visualization of anatomical structures (Z = −3.903, *p* < 0.001). There were more artefacts detected on 3D-FSE-Cube (Figure 6b,d), as compared to 3D-FSE-Cube-Flex

Figure 6. Example image of a 22-year-old female volunteer, in which the maxillary sinus was filled with gas. The reformatted coronal (a) and oblique sagittal planes (c) of NLD (swallowtail arrows) on 3D-FSE-Cube-Flex; and reformatted coronal (b) and oblique sagittal planes (d) of NLD on 3D-FSE-Cube for the same subject. 3D-FSE-Cube-Flex MRD demonstrated minimal and serrated artefacts, but there were more columnar artefacts with 3D-FSE-Cube. 3D-FSE, three-dimensional-fast spin-echo; NLD, nasolacrimal duct.

(Figure 6a,c) (Z = −5.321, p < 0.001). There was no pronounced statistical difference between sharpness for the paired images (Z = −1.414, p = 0.157), although the lacrimal duct wall appeared more blurred on 3D-FSE-Cube-Flex images (Table 2).

Inter-reader agreement was (almost) perfect for all metrics, the κ (intraclass correlation coefficient) value range from 0.737 to 0.996 (Table 3).

DISCUSSION

Since the Dixon method was first proposed in 1984,[22] its variants have used chemical shift fat-saturation with a post-processing phase correction during the reconstruction process to eliminate the effect of field inhomogeneities. Flex is a modified 2-point Dixon technique that acquires two echoes (one in-phase and one out-of-phase, with respect to water and fat), for each phase encode step. Using the two echoes and a robust phase correction

algorithm, the B0 inhomogeneity map is estimated and later demodulated from the source images to separate water and fat images completely. The 3D-FSE-Cube-Flex technique is an integration of the 3D-FSE volumetric acquisition with the modified two-point Dixon water-fat separation method with flexible echo times. Cube-Flex consists of three steps: using a flexible dual-echo Cube-T2 acquisition with two-dimensional accelerated autocalibrating reconstruction for cartesian parallel imaging for acquisition. Then, the un-acquired phase and slice encoding for each echo are synthesized using the autocalibrating reconstruction for cartesian reconstruction algorithm. Finally, four data sets are generated using the post-processing algorithm: water-only images, fat-only images, in-phase images, out-of-phase images. The novelty regarding this method is the implementation of the phase-correction algorithm based on a region-growing scheme, but without usual constraints on the echo times.[23] In addition, Cube-Flex can use bipolar readouts to acquire three different

Table 2. Qualitative assessment, comparison between 3D-FSE-Cube-Flex MRD and 3D-FSE-Cube MRD for ratings of artefacts, sharpness, overall image quality and visualization of anatomical structures

Parameters	Rating					Total	Significance
	Flex << cube	Flex < cube	Flex = cube	Flex > cube	Flex >> cube		
Artefact	18	17	7	0	0	42	Flex less than cube, $p < 0.001$
Sharpness	1	17	13	11	0	42	Flex less than cube, $p = 0.157^*$
Overall image quality	0	4	10	15	13	42	Flex better than cube, $p < 0.001$
Visualization of anatomy	0	3	16	15	8	42	Flex better than cube, $p < 0.001$

Flex, 3D-FSE-Cube-Flex MRD; Cube, 3D-FSE-Cube MRD.
A two-tailed paired-sample Wilcoxon signed-rank test was utilized to compare and analyze the difference in the above quality metric.
$p < 0.05$ was considered statistically significant.
"<<" is equal to a score of −2, "<" equals to a score of −1, "=" equals to a score of 0, ">" is equal to a score of 1, ">>" is equal to a score of 2.

echo times for fat–water separation within a single pass, using a technique known as Fast Triple Echo Dixon (FTED). Ma et al[24] had previously reported that the FTED technique provided higher image quality *in vivo* with uncompromised scan parameters than with conventional FSE sequences with CHESS fat suppression. As Jong et al[25] has mentioned, the flexible FTED technique incorporates the benefits of both FSE and Dixon imaging and provides more flexibility in applications such as fat suppressed T_2-weighted imaging. With FTED methods, for data acquisition each readout gradient along the echo train of the FRFSE sequences is replaced with three successive readout gradients of alternating polarity. The corresponding three echoes generate three raw images at a relative phase angle of -θ, 0°, and θ between the water and fat signals, where θ is flexible and no longer limited to 180°. The region growing-based two-point Dixon phase correction algorithm is used to joint process two separate pairs of raw images (one set of water-only and fat-only images from the -θ and 0° raw images and another set of water-only and fat-only images from the 0° and +θ raw images).[26]

When properly added together, this single-pass mode accelerates and increases SNR efficiency of Flex applications, yielding a final water-only image, and a final fat-only image, with improved SNR and CNR performance.

In this study, the 3D-FSE-Cube-Flex MRD achieved statistically higher SNR and CNR in comparison with that of the 3D-FSE-Cube. On one hand, this phenomenon may be attributed to parallel acceleration imaging used in 3D-FSE-Cube, which decreases the SNR while reducing scan time. However, the Dixon method can easily compensate this effect due to multiple point acquisition.[27–29] On the other hand, we found that although the average SI of the liquid on the 3D-FSE-Cube image was higher than that of Cube-Flex, background noise was better suppressed on the latter sequence, which completely compensates for the strength of the fluid signal decline. We principally evaluated the artefacts occurring in the lower LDS that result from the non-uniform magnetic field, which can be diminished by optimizing imaging parameters. Due to a lower sensitivity to field

Table 3. Interobserver agreement for quantitative and grading parameters

Parameters	Cube-Flex		Cube	
	ICC/κ	95% CI	ICC/κ	95% CI
SNR	0.996^a	0.993–0.998	0.995^a	0.991–0.997
CNR	0.992^a	0.985–0.996	0.995^a	0.990–0.997
SC	0.765	0.603–0.928	0.758	0.603–0.913
IC	0.77	0.505–0.902	0.79	0.595–0.897
CC	0.843	0.645–0.935	0.855	0.711–0.930
LS	0.961	0.917–0.982	0.947	0.871–0.979
NLD	0.878	0.774–0.922	0.914	0.843–0.938
Artefact	0.892	0.857–0.918	0.815	0.675–0.954
Sharpness	0.783	0.655–0.911	0.763	0.536–0.899
Overall image quality	0.804	0.603–0.913	0.809	0.675–0.942
Visualization of anatomy	0.737	0.57–0.903	0.764	0.614–0.913

ICC, intraclass correlation coefficient; CI, confidence interval;CC, common canaliculus; IC, inferior canaliculus; LS, lacrimal sac; NLD, nasolacrimal duct; CNR, contrast-to-noise ratio; SNR, signal-to-noise ratio;
[a]Based on ICC method, the others were analysed by Kappa methods.

inhomogeneity and the utilization of FTED technique, our experience confirms that MRD using the 3D-FSE-Cube-Flex sequence can achieve higher quality fat-suppression images, and less vulnerability to field inhomogeneity artefacts than the 3D-FSE-Cube sequence. Multiple columnar artefacts frequently appeared with the 3D-FSE-Cube sequence, which can affect the continuity of NLD visualization. In contrast, there were far less artefacts on 3D-FSE-Cube-Flex MRD images, which improved the visualization of the lower LDS segments, especially the NLDs.

In order to achieve different water–fat phase shifts, as required in the Dixon method postprocessing, the minimum echo spacing must be increased, which can result in increased image blurring due to larger T2 decay.[29,30] In addition, to ensure consistency in scan time for both sequences, we reduce the number of excitations on for the 3D-FSE-Cube-Flex, which leaded to lower SI and image contrast for fine structures when compared to 3D-FSE-Cube acquisitions. Although there was no significant difference, a slightly decrease in anatomic sharpness is observed on the FTED (3D-FSE-Cube-Flex) images, which is consistent with the report of Russell et al.[26] The 3D-FSE-Cube-Flex MRD showed better overall image quality and anatomical visualization, which may result in a less noisy background, robust water-fat suppression, and less artefacts.

In this study, the visibility scores for the upper drainage segments (SC, IC, and CC) were relatively higher with 3D-FSE-Cube MRD. This may be explained by the longer repetition time, resulting in the fluid-filled canaliculus achieving full relaxation and obtaining a heavier T_2 weighting. As previously described, the measured value of liquid signals using 3D-FSE-Cube are significantly higher than those of Cube-Flex. In addition, the shorter echo spacing was accompanied with decreased blurring on 3D-FSE-Cube imaging, with the effect being more pronounced on the slender superior lacrimal passage. Moreover, the tissue surrounding the superior LDS is relatively more homogeneous than that of the lower segments, which produces less inhomogeneity artefacts in the superior LDS region. Therefore, these comprehensive effects generated higher subjective rating scores for the superior LDS on 3D-FSE-Cube MRD. As for the lower LDS segments, the foregoing results displayed higher CNR and SNR on 3D-FSE-Cube-Flex.Furthermore, efficient fat-suppression methods mitigate inhomogeneity artefacts, which is one of the most serious problems affecting rating score, hence, the 3D-FSE-Cube Flex received higher scores for visibility of the lower LDS.

The main limitation of the current research is that the parameter settings were based on identical acquisition times, as partial parameters were not strictly matched, and the optimization of 3D-FSE-Cube-Flex MRD remains a work in progress. Some examples of parameter optimization include the number of excitations and the receiver bandwidth being selected using a more advanced technique, which may also improve the image quality. Another limitation is that only asymptomatic volunteers were enrolled, and all image performance was based on normal drainage and excretion function of the LDS. Therefore, a larger investigation will be necessary to evaluate the 3D-FSE-Cube-Flex MRD images for specific LDS-related disease, such as epiphora and to translate into image improvements in disease detection.

In conclusion, 3D-FSE-Cube-Flex MRD coupled with a two-point, fat-water separation based on the FTED technique is a promising technique, when compared to the 3D-FSE-Cube MRD routine fat suppression, thereby providing homogeneous fat suppression, artefact reduction, and noticeable improvements in image quality of the lower LDS. Nevertheless, 3D-FSE-Cube MRD provided less than optimal images of the upper LDS. The mutual implementation of these methods may replace the currently used 3D hydrographic MRD, as well as other routine sequences, which can simplify diagnostic imaging workflow and improve examine efficiency.

ACKNOWLEDGMENT

REFERENCES

1. Busse H, Müller KM, Kroll P, Radiological KP, Findings.pdf H. Radiological and histological findings of the lacrimal passages of newborns. *Arch Ophthalmol* 1980; **98**: 528–32. doi: https://doi.org/10.1001/archopht.1980.01020030524019

2. Maliborski A, Różycki R. Diagnostic imaging of the nasolacrimal drainage system. Part I. Radiological anatomy of lacrimal pathways. Physiology of tear secretion and tear outflow. *Med Sci Monit* 2014; **20**: 628–38. doi: https://doi.org/10.12659/MSM.890098

3. Caldemeyer KS, Stockberger SM, Broderick LS. Topical contrast-enhanced CT and MR dacryocystography: imaging the lacrimal drainage apparatus of healthy volunteers. *AJR Am J Roentgenol* 1998; **171**: 1501–4. doi: https://doi.org/10.2214/ajr.171.6.9843278

4. Yoshikawa T, Hirota S, Sugimura K. Topical contrast-enhanced magnetic resonance dacryocystography. *Radiat Med* 2000; **18**: 355–62.

5. Somma F, d'Agostino V, Tortora F, Serra N, Sorrentino G, Piscitelli V, et al. Magnetic resonance imaging in the preoperative evaluation of obstructive epiphora: true-FISP and VIBE vs gadolinium. *Radiol Med* 2017; **122**: 123–30. doi: https://doi.org/10.1007/s11547-016-0696-4

6. Zhang J, Chen L, Wang QX, Liu R, Zhu WZ, Luo X, et al. Diagnostic performance of the three-dimensional fast spin echo-Cube sequence in comparison with a conventional imaging protocol in evaluation of the lachrymal drainage system. *Eur Radiol* 2015; **25**: 635–43. doi: https://doi.org/10.1007/s00330-014-3462-9

7. Jing Z, Lang C, Qiu-Xia W, Rong L, Xin L, Wen-Zhen Z, et al. High-spatial-resolution isotropic three-dimensional fast-recovery fast spin-echo magnetic resonance dacryocystography combined with topical administration of sterile saline solution. *Eur*

J Radiol 2013; **82**: 1546–51. doi: https://doi.org/10.1016/j.ejrad.2013.04.013

8. Zhang J, Chen L, Wang QX, Liu R, Zhu WZ, Luo X, et al. Isotropic three-dimensional fast spin-echo Cube magnetic resonance dacryocystography: comparison with the three-dimensional fast-recovery fast spin-echo technique. *Neuroradiology* 2015; **57**: 357–65. doi: https://doi.org/10.1007/s00234-014-1484-2

9. Haase A, Frahm J, Hänicke W, Matthaei D. 1H NMR chemical shift selective (CHESS) imaging. *Phys Med Biol* 1985; **30**: 341–4. doi: https://doi.org/10.1088/0031-9155/30/4/008

10. Frahm J, Haase A, Hänicke W, Matthaei D, Bomsdorf H, Helzel T. Chemical shift selective MR imaging using a whole-body magnet. *Radiology* 1985; **156**: 441–4. doi: https://doi.org/10.1148/radiology.156.2.4011907

11. Cornfeld DM, Israel G, McCarthy SM, Weinreb JC. Pelvic imaging using a T1W fat-suppressed three-dimensional dual echo Dixon technique at 3T. *J Magn Reson Imaging* 2008; **28**: 121–7. doi: https://doi.org/10.1002/jmri.21402

12. Madhuranthakam AJ, Smith MP, Yu H, Shimakawa A, Reeder SB, Rofsky NM, et al. Water-silicone separated volumetric MR acquisition for rapid assessment of breast implants. *J Magn Reson Imaging* 2012; **35**: 1216–21. doi: https://doi.org/10.1002/jmri.22872

13. Ma J. Breath-hold water and fat imaging using a dual-echo two-point Dixon technique with an efficient and robust phase-correction algorithm. *Magn Reson Med* 2004; **52**: 415–9. doi: https://doi.org/10.1002/mrm.20146

14. Saito S, Tanaka K, Hashido T. Liver acquisition with volume acceleration flex on 70-cm wide-bore and 60-cm conventional-bore 3.0-T MRI. *Radiol Phys Technol* 2016; **9**: 154–60. doi: https://doi.org/10.1007/s12194-015-0344-z

15. Guerini H, Omoumi P, Guichoux F, Vuillemin V, Morvan G, Zins M, et al. Fat Suppression with Dixon Techniques in Musculoskeletal Magnetic Resonance Imaging: A Pictorial Review. *Semin Musculoskelet Radiol* 2015; **19**: 335–47. doi: https://doi.org/10.1055/s-0035-1565913

16. Ma J, Singh SK, Kumar AJ, Leeds NE, Zhan J. T2-weighted spine imaging with a fast three-point dixon technique: comparison with chemical shift selective fat suppression. *J Magn Reson Imaging* 2004; **20**: 1025–9. doi: https://doi.org/10.1002/jmri.20201

17. McMahon CJ, Madhuranthakam AJ, Wu JS, Yablon CM, Wei JL, Rofsky NM, et al. High-resolution proton density weighted three-dimensional fast spin echo (3D-FSE) of the knee with IDEAL at 1.5 Tesla: comparison with 3D-FSE and 2D-FSE--initial experience. *J Magn Reson Imaging* 2012; **35**: 361–9. doi: https://doi.org/10.1002/jmri.22829

18. Stevens KJ, Busse RF, Han E, Brau AC, Beatty PJ, Beaulieu CF, et al. Ankle: isotropic MR imaging with 3D-FSE-cube--initial experience in healthy volunteers. *Radiology* 2008; **249**: 1026–33. doi: https://doi.org/10.1148/radiol.2493080227

19. Wang X, Harrison C, Mariappan YK, Gopalakrishnan K, Chhabra A, Lenkinski RE, et al. MR Neurography of Brachial Plexus at 3.0 T with Robust Fat and Blood Suppression. *Radiology* 2017; **283**: 538–46. doi: https://doi.org/10.1148/radiol.2016152842

20. Samji K, Alrashed A, Shabana WM, McInnes MD, Bayram E, Schieda N. Comparison of high-resolution T1W 3D GRE (LAVA) with 2-point Dixon fat/water separation (FLEX) to T1W fast spin echo (FSE) in prostate cancer (PCa). *Clin Imaging* 2016; **40**: 407–13. doi: https://doi.org/10.1016/j.clinimag.2015.11.023

21. Del Grande F, Santini F, Herzka DA, Aro MR, Dean CW, Gold GE, et al. Fat-suppression techniques for 3-T MR imaging of the musculoskeletal system. *Radiographics* 2014; **34**: 217–33. doi: https://doi.org/10.1148/rg.341135130

22. Dixon WT. Simple proton spectroscopic imaging. *Radiology* 1984; **153**: 189–94. doi: https://doi.org/10.1148/radiology.153.1.6089263

23. Eggers H, Brendel B, Duijndam A, Herigault G. Dual-echo Dixon imaging with flexible choice of echo times. *Magn Reson Med* 2011; **65**: 96–107. doi: https://doi.org/10.1002/mrm.22578

24. Ma J, Son JB, Zhou Y, Le-Petross H, Choi H. Fast spin-echo triple-echo dixon (fTED) technique for efficient T2-weighted water and fat imaging. *Magn Reson Med* 2007; **58**: 103–9. doi: https://doi.org/10.1002/mrm.21268

25. Son JB, Hwang KP, Madewell JE, Bayram E, Hazle JD, Low RN, et al. A flexible fast spin echo triple-echo Dixon technique. *Magn Reson Med* 2017; **77**: 1049–57. doi: https://doi.org/10.1002/mrm.26186

26. Low RN, Austin MJ, Ma J. Fast spin-echo triple echo dixon: Initial clinical experience with a novel pulse sequence for simultaneous fat-suppressed and nonfat-suppressed T2-weighted spine magnetic resonance imaging. *J Magn Reson Imaging* 2011; **33**: 390–400. doi: https://doi.org/10.1002/jmri.22453

27. Pruessmann KP, Weiger M, Scheidegger MB, Boesiger P. SENSE: sensitivity encoding for fast MRI. *Magn Reson Med* 1999; **42**: 952–62. doi: https://doi.org/10.1002/(SICI)1522-2594(199911)42:5<952::AID-MRM16>3.0.CO;2-S

28. Sodickson DK, Manning WJ. Simultaneous acquisition of spatial harmonics (SMASH): fast imaging with radiofrequency coil arrays. *Magn Reson Med* 1997; **38**: 591–603. doi: https://doi.org/10.1002/mrm.1910380414

29. Ma J. Dixon techniques for water and fat imaging. *J Magn Reson Imaging* 2008; **28**: 543–58. doi: https://doi.org/10.1002/jmri.21492

30. Sze G, Kawamura Y, Negishi C, Constable RT, Merriam M, Oshio K, et al. Fast spin-echo MR imaging of the cervical spine: influence of echo train length and echo spacing on image contrast and quality. *AJNR Am J Neuroradiol* 1993; **14**: 1203–13.